

Determination of Magnetic Symmetries by Convergent Beam Electron Diffraction

O. Zaiets,^{1,2,*} C. Timm,^{3,4} J. Ruzs,⁵ J.-Á. Castellanos-Reyes,⁵ S. Subakti,¹ and A. Lubk^{1,2,4,†}

¹*Leibniz Institute for Solid State and Materials Research Dresden, Helmholtzstraße 20, 01069 Dresden, Germany*

²*Institute of Solid State and Materials Physics, TU Dresden, Haeckelstraße 3, 01069 Dresden, Germany*

³*Institute of Theoretical Physics, TU Dresden, 01062 Dresden, Germany*

⁴*Würzburg–Dresden Cluster of Excellence ct.qmat, TU Dresden, 01062 Dresden, Germany*

⁵*Department of Physics and Astronomy, Uppsala University, 75120 Uppsala, Sweden*

Convergent-beam electron diffraction (CBED) is a well-established probe for spatial symmetries of crystalline samples, mainly exploiting the well-defined mapping between the diffraction groups (symmetry group of CBED patterns) and the point-group symmetries of the crystalline sample. In this work, we extend CBED to determine magnetic point groups. We construct all magnetic CBED groups, of which there exist 125. Then, we provide the complete mapping of the 122 magnetic point groups to corresponding magnetic CBED groups for all crystal orientations. In order to verify the group-theoretical considerations, we conduct electron-scattering simulations on antiferromagnetic crystals and provide guidelines for the experimental realization. Based on its feasibility using existing technology, as well as on its accuracy, high spatial resolution, and small required sample size, magnetic CBED promises to become a valuable alternative method for magnetic structure determination.

I. INTRODUCTION

Symmetry has always played an important role in the fundamental understanding and prediction of physical phenomena. In particular, Neumann’s principle for solid-state physics connects structural point-group or space-group symmetry of a crystal with the symmetry of its physical properties, such as dielectric, piezoelectric, and elastic linear response tensors. By extension, this principle also holds for magnetic properties, which raises the need for experimental methods for determining symmetries of crystals incorporating the magnetic structure. We introduce a novel comprehensive method for probing magnetic symmetries in magnetically ordered crystalline matter (i.e., ferro-, ferri-, and antiferromagnets) by leveraging electron-diffraction techniques employing a Transmission Electron Microscope (TEM). Its simplicity, spatial resolution down to ten nanometers, and cost-effectiveness are suited to drastically expand the scope of magnetic-symmetry determination currently carried out by neutron diffraction.

Magnetic point and space groups [1], also referred to as Shubnikov groups, provide a fundamental classification underlying all magnetic or spin-related properties of crystalline solids [2], such as ferro-, ferri- and antiferromagnetism [3], altermagnetism [4], topological insulation [5], and semimetallicity [6, 7]. Magnetic space groups extend the crystallographic space groups by combining spatial symmetries with time-reversal symmetry, which connects opposite spin orientations, and provide compatibility conditions for magnetic properties following Neumann’s principle. Therefore, experimental probes of magnetic point-group and space-group symmetries, analogous to probes of crystallographic symmetries, are

indispensable for studies of solid-state magnetism, with neutron diffraction being the main probe [8]. A direct determination of the magnetic symmetry from the symmetries of a neutron diffraction pattern is, however, hampered by Friedel’s law that holds for scattering within the Born approximation: Opposite reflections in a neutron diffraction pattern are always symmetric even for non-centrosymmetric space groups. Motivated by this and other limits of neutron diffraction, such as limited spatial resolution and relatively large required crystal sizes, we establish an alternative technique based on electron diffraction in this paper. We introduce a method for the determination of magnetic point groups that allows direct measurement of symmetries with a spatial resolution reaching several nanometers, referred to as “magnetic convergent-beam electron diffraction.”

Convergent-beam electron diffraction (CBED) is a transmission-electron-microscopy (TEM) technique that focuses, i.e., converges, an electron beam, typically of 60–300 kV acceleration voltage, to spot sizes of the order of 10 nanometers on a thin TEM sample slab and records the transmitted diffraction pattern of Bragg disks [9–11], see Fig. 1. Such CBED patterns have their own specific diffraction symmetries, i.e., mirror or rotational symmetries, which depend on structural symmetry groups and the zone-axis orientation of the TEM sample slab [12, 13]. More specifically, the CBED patterns directly inherit the point-group symmetries of the scattering potential of the TEM sample slab. Additional Friedel pair symmetries are not present because electron scattering on crystalline samples typically falls outside of the Born approximation regime [14]. In other words, the beam electrons scatter multiple times—also referred to as dynamical scattering—instead of just once, as described by the first Born approximation and also referred to as kinematical scattering. Opposite reflections then lose their symmetry in non-centrosymmetric scattering potentials because of the non-symmetric intermediate scattering phases of

* o.zaiets@ifw-dresden.de

† a.lubk@ifw-dresden.de

the diffracted beams. The point-group symmetries of the TEM sample slab are given by the intersection of the original bulk crystal symmetries with the geometric symmetries of the slab. In other words, all crystal symmetries acting on the normal direction of the slab, referred to as z in the following, are broken with the notable exception of z -reversal, i.e., mirror symmetry with respect to xy -plane at the center of the slab, and combinations of z -reversal with in-plane point group symmetries. Therefore, the CBED symmetry of a slab of particular orientation corresponds to the in-plane crystallographic symmetries of the slab plus possible z -reversal symmetries, including combinations of in-plane and z -reversal symmetries. This stipulates a well-defined mapping between CBED pattern symmetries and structural point-group symmetries [12], which may be uniquely inverted provided that a sufficient number of CBED patterns of slabs in various zone-axis orientations is recorded. Numerous studies have employed this inverse mapping to study symmetries of crystalline matter down to very small length scales [15–20], revealing the presence of strain, ferroelectric polarization, or chirality. An extension of this mapping to space-group symmetries requires considerable effort regarding the incompatibility of slab symmetries with translational symmetries in the z direction. Although we will touch upon this topic below, our main focus in this work is on point-group symmetries.

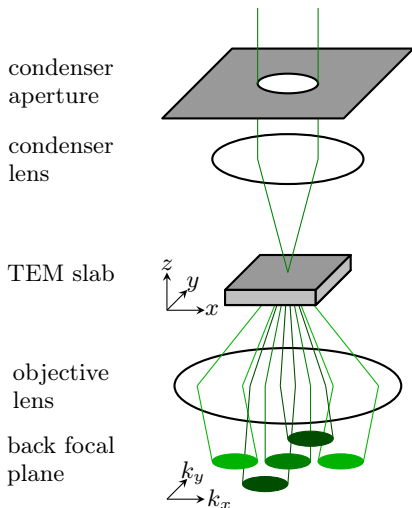


FIG. 1. Minimal optical model of a CBED setup. The beam converges in the sample plane, while the beam-limiting aperture is in the front focal plane of the condenser lens. The CBED pattern is recorded in the back focal plane (far field), where diffracted beams appear as disks because of the convergent illumination. Sample space as well as focal plane (far field) coordinates are indicated.

While the conventional CBED technique focuses solely on structural symmetries of the crystal imprinted on the electrostatic scattering potential, a growing number of electron-scattering studies highlight the impact of the magnetic field. In an early study, Shen and Laughlin [21]

showed the breaking of structural CBED symmetries by the presence of the strong uniaxial permanent magnetic field in ferromagnetic PrCo_5 . Later, Loudon [22] revealed the existence of purely magnetic electron-diffraction spots in parallel-beam electron diffraction on antiferromagnetic NiO , where the antiferromagnetic unit cell is doubled compared to the structural one. This work paved the way for the detection of antiferromagnetic order in the Transmission Electron Microscope. Recently, Kohno *et al.* [23] demonstrated the sensitivity of atomic-resolution differential phase contrast (another convergent-beam electron-diffraction technique, where first moments of diffraction patterns are analyzed) to the antiferromagnetic structure of Fe_2O_3 . These and similar observations [24–26] suggest the experimental possibility to detect the generally weak electron-diffraction effects due to atomic magnetic fields [27]. The latter is the main goal for the following generalization of the conventional CBED symmetry analysis by taking into account symmetries of the magnetic crystal structure.

II. ELECTRON DIFFRACTION AT ELECTRIC AND MAGNETIC POTENTIALS

Electron beams accelerated by voltages in the 60 kV to 300 kV range attain relativistic velocities (e.g., $v \approx 0.8c$ at 300 kV acceleration voltage) and are predominantly scattered by very small angles (less than 100 mrad) relative to the optical axis in a transmission electron microscope. In this small-angle, or paraxial scattering, limit, the effects of spin through spin-orbit coupling and Zeeman coupling are negligible, meaning the spinor nature of the electron wave function can be ignored. As a result, spin does not influence the diffraction, allowing us to treat the electron’s wave function as a scalar. Moreover, the resulting scalar wave function ψ may be decomposed into a fast carrier wave function and an envelope wave function Ψ that is slowly varying along the optical axis, i.e., $\psi(\mathbf{r}_\perp, z) = e^{ik_0z} \Psi(\mathbf{r}_\perp, z)$ with $\mathbf{r}_\perp = (x, y)$ denoting the in-plane slab coordinates and k_0 the wave number of the fast carrier wave. Here, the time-dependent oscillation has already been separated, i.e., we only consider eigensolutions with a certain electron energy E . Inserting the above decomposition into the Klein-Gordon equation for scalar relativistic particles and neglecting a couple of terms that are small due to the high beam energy, the evolution of the envelope wave function along the optical axis can be described by the paraxial Schrödinger equation [28, 29] (see Appendix A for a detailed derivation)

$$i \frac{\partial \Psi}{\partial z} = \left(\frac{1}{2k_0} \left(i \nabla_\perp + \frac{e}{\hbar} \mathbf{A}_\perp \right)^2 + \frac{e}{\hbar} A_z - \frac{e}{\hbar v} \Phi \right) \Psi \equiv \hat{H}_\perp \Psi, \quad (1)$$

where e is the elementary charge, $\mathbf{A} = (\mathbf{A}_\perp, A_z)$ the vector potential, and Φ the scalar potential. Spatial arguments of potentials and envelope wave function have

been omitted in order to simplify the notation. The vector potential is fixed by the Coulomb gauge in the following considerations and generally leads to effects several orders of magnitude smaller than the diffraction due to the scalar potential. As a consequence of the large wave vector of the fast-beam electrons, one may further simplify the above equation by neglecting in-plane vector-potential terms containing \mathbf{A}_\perp .

The symmetries of the solution of the above equation in the absence of the vector potential, $\mathbf{A} = 0$, have been exploited for structural symmetry determination using CBED based on the following argument. A CBED pattern corresponds to the absolute square of the electron wave function in the far field behind the object (coordinates $\mathbf{k}_\perp = (k_x, k_y)^T$). Therefore, the CBED discs appear at integer multiples of unit vectors of the crystal's reciprocal lattice according to Bragg's law, see Fig. 1. The electron wave function, on the other hand, inherits symmetries from the paraxial Hamiltonian \hat{H}_\perp and hence symmetries of the electric scattering potential Φ , which leads to a direct relationship between symmetries of the latter and those of the CBED pattern [30]. Given the similar mathematical structure of the above equation with and without magnetic vector potential, this reasoning may be also adopted to derive the relationship between CBED pattern symmetries and magnetic point-group symmetries with the important extension that we need to include time-reversal symmetry.

The structure of Eq. (1) corresponds to a two-dimensional time-dependent Schrödinger equation, i.e., a $(2+1)$ -dimensional theory, with z and the paraxial Hamiltonian \hat{H}_\perp taking the place of the time coordinate and the usual Hamiltonian, respectively [31, 32]. In the following, we will take advantage of this analogy, allowing for a substantial portion of the time-dependent Schrödinger equation's properties and solutions to be transferred to paraxial scattering.

The full solution of the paraxial equation (1) for a given initial wave at the entrance plane z_0 of the slab can be formally obtained as

$$\Psi(z) = Z \exp \left(\underbrace{-i \int_{z_0}^z dz' \hat{H}_\perp(z')}_{\equiv \hat{K}(z, z_0)} \right) \Psi(z_0), \quad (2)$$

where Z denotes the z -ordering directive in analogy to Dyson's time-ordering directive and $\hat{K}(z, z_0)$ is the z -evolution operator (or propagator) corresponding to the time-evolution operator. The intensity $I(\mathbf{k}_\perp)$ recorded in a CBED pattern is obtained by applying the propagator to the wave function, i.e., the convergent probe beam, in reciprocal space,

$$I(\mathbf{k}_\perp) = \left| \iint d^2k'_\perp \hat{K}(\mathbf{k}_\perp, z, \mathbf{k}'_\perp, z_0) \Psi(\mathbf{k}'_\perp, z_0) \right|^2. \quad (3)$$

In full analogy to time evolution, the z evolution is unitary, conserving the norm of the wave function along z ,

because the Hamiltonian H_\perp is hermitian. Moreover, any in-plane symmetries (rotations, mirror reflections, and translations in the xy plane) leave the propagator invariant because the corresponding unitary symmetry transformations \hat{T}_\perp commute with the Hamiltonian \hat{H}_\perp and hence with the propagator, $[\hat{T}_\perp, \hat{K}] = 0$. Translational symmetries correspond to phase factors in reciprocal space, which are not directly visible as diffraction symmetries but instead lead to absences of diffraction peaks. Hence, only in-plane rotation and mirror symmetries, i.e., the in-plane point group symmetry of the slab, translate to symmetries of the CBED pattern.

Another notable analogy between the two-dimensional time-dependent and the paraxial z -dependent Schrödinger equations concerns the reversal of the propagation parameter. Time reversal corresponds to an antiunitary operator consisting of complex conjugation of the scalar wave function. The same complex conjugation is applied to the envelope wave function under z reversal, which can be shown along the same lines as for the time-dependent Schrödinger equation. Moreover, if the paraxial Hamiltonian \hat{H}_\perp is z -reversal invariant, the propagator and hence the CBED pattern will remain the same after z reversal of the slab if the following important condition is fulfilled: The upper and lower face of the slab need to be identical crystal planes. If this condition is not satisfied the crystal slab breaks z -reversal symmetry even if the bulk crystal has this symmetry.

In addition, the presence of non-zero magnetization and vector potential gives rise to another symmetry operation—magnetization or time reversal—inherited by the CBED pattern. The full symmetries, including time reversal, of the CBED patterns of a magnetic sample may be obtained by the same logic than those of non-magnetic ones. We start from the magnetic space group symmetries of the crystal. The slab geometry breaks spatial symmetries involving z , possibly except for z -reversal, and imprints these symmetries onto the CBED pattern recorded along the normal axis of the slab. Exploiting this principle, magnetic CBED in a Transmission Electron Microscope can be a viable alternative to neutron diffraction for the determination of magnetic point groups of magnetic samples provided that the mapping of magnetic CBED symmetry groups (also referred to as magnetic diffraction groups (DG)) to magnetic point groups can be worked out and the presence of magnetic CBED symmetries can be determined experimentally.

In the following, we construct the complete magnetic CBED group (magnetic DG) from group-theoretical principles and provide the complete mapping between magnetic CBED groups and magnetic point groups. We then conduct scattering simulations involving numerical solutions of Eq. (1) for antiferromagnetic samples in order to verify the theory. Subsequently, we discuss the experimental challenges for implementing magnetic CBED.

III. MAGNETIC CBED GROUPS

In this section, we discuss the possible point groups of magnetic CBED patterns. Details and lists of all groups are relegated to Appendix B. The construction relies on the following main assumptions: (a) Time reversal and z reversal both act as antiunitary transformations, as explained in Sec. II. (b) Both square to the identity since fermionic properties of electrons can be disregarded for relativistic beams. This point has also been discussed in Sec. II. In other words, we do not require double groups. (c) Time reversal and z reversal commute with all other structural point-group transformations. (d) The two also commute with each other.

Starting from the magnetic point group of the bulk crystal, we first need to construct the subgroup of elements that leave the slab geometry invariant, as discussed in Sec. II. This leads to the 10 two-dimensional structural point groups, in Schoenflies notation, C_n and D_n with $n = 1, 2, 3, 4, 6$. It is easy to check explicitly that all elements of these groups commute with z reversal. The fact that z reversal is antiunitary does not affect the commutation relations [33]. Time reversal commutes with all possible structural transformations in any case [34]. These arguments justify assumptions (c) and (d).

Including the antiunitary time-reversal operation \mathcal{T} leads to 31 two-dimensional magnetic point groups in total [35]: First, the 10 groups, G , noted above, which do not contain time reversal and are called “monochromatic.” Second, 10 groups $G + G\mathcal{T}$, which result from adding time reversal \mathcal{T} as a generator. These groups are called “gray.” Third, 11 groups that are created by identifying a halving subgroup H of a monochromatic group G and forming the group $H + (G \setminus H)\mathcal{T}$, i.e., by multiplying the coset $G \setminus H$ by time reversal. These groups are called “dichromatic.” For an introduction to magnetic point groups see, for example, [36, 37].

We now denote the antiunitary reversal of the z coordinate by \mathcal{Z} . This operation is antiunitary, squares to the identity, and commutes with all other structural symmetry operations. Hence, \mathcal{Z} and \mathcal{T} have the same algebraic properties and the theory of point groups including \mathcal{Z} is analogous to the theory of point groups including \mathcal{T} . Thus by including \mathcal{Z} but not \mathcal{T} , we obtain 10 “ \mathcal{Z} gray” groups and 11 “ \mathcal{Z} dichromatic” groups.

Novel possibilities arise if \mathcal{T} and \mathcal{Z} are both present, either by themselves or only in combination with structural transformations or with each other. The latter combination, which we denote by

$$\Omega \equiv \mathcal{T}\mathcal{Z} = \mathcal{Z}\mathcal{T}, \quad (4)$$

is *unitary*. The properties of \mathcal{T} and \mathcal{Z} imply that Ω squares to the identity and commutes with all possible group elements.

For any of the 10 structural groups G , we can now construct CBED groups by applying one or more of the following steps:

(1) We can add one of the operations \mathcal{T} , \mathcal{Z} , or Ω as a new generator. We can also add two of them as new generators. Since the product of any two operations is the third one, this only produces 10 additional groups $G + G\mathcal{T} + G\mathcal{Z} + G\Omega$. These groups are both \mathcal{T} gray and \mathcal{Z} gray.

(2) If G has a halving subgroup H , then its coset $G \setminus H$ can be multiplied by one of the operations \mathcal{T} , \mathcal{Z} , or Ω .

(3) If G has two distinct halving subgroups H_1 and H_2 , then the corresponding cosets $G \setminus H_1$ and $G \setminus H_2$ can be multiplied by two distinct operations out of $\{\mathcal{T}, \mathcal{Z}, \Omega\}$.

As detailed in Appendix B, we end up with 125 magnetic CBED groups in total. Table I summarizes the results. We conclude this section with two remarks: First, two groups can be distinct even if they have the same structure, i.e., correspond to the same formal group. For example, the groups C_2 and D_1 correspond to the same formal group but are distinct because the symmetry transformation involved is physically different—a rotation and a mirror reflection, respectively. Second, the orders of the groups are easily read off from the second column, noting that H is a halving subgroup of G and Q is a quartering subgroup of G .

IV. RELATION BETWEEN MAGNETIC CBED GROUPS AND MAGNETIC POINT GROUPS

The group-theoretical considerations in Sec. III have provided a list of all 125 magnetic CBED groups possible by combining two-dimensional structural point-group symmetry operations with time reversal (and thus magnetization reversal) and z reversal. The missing piece required for determining magnetic point groups from CBED measurements is a mapping from the 122 three-dimensional magnetic point groups of magnetic materials to the 125 magnetic CBED groups, which we will provide in this section, with all mappings tabulated in Appendix C.

When the electron beam is scattered by the thin TEM sample, the magnetic point-group symmetry is broken by the TEM slab geometry as discussed in Sec. II. An example for the case of magnetic point group $4'/m$ is presented in Fig. 2. Here, the prime denotes time reversal as usual. This group is generated by the fourfold rotation about the principal axis multiplied by time reversal, $4'$, and the reflection in the mirror plane perpendicular to that axis, m .

We first consider a slab with surface normal oriented along the [001] crystallographic axis, i.e., the fourfold symmetry axis. Thus, this slab orientation is compatible with the point group $4'/m$. The mirror reflection in the horizontal plane is then mapped to the z -reversal symmetry, which we denote by 1_R , following the conventions from CBED literature [12]. The corresponding magnetic CBED group is thus $4'1_R$.

On the other hand, a slab with normal along $[2\bar{1}0]$ is incompatible with all operations that involve rotations

TABLE I. Summary of CBED groups. The construction, the resulting type of the groups, and their number is shown. $G \in \{C_n, D_n | n = 1, 2, 3, 4, 6\}$ is a structural point group, H is a halving subgroup of G , and Q is a quartering subgroup of G , i.e., a halving subgroup of a halving subgroup. Moreover, \mathcal{T} denotes time reversal, \mathcal{Z} denotes z reversal, and $\Omega = \mathcal{T}\mathcal{Z}$ denotes their product. c_n denotes the highest-order rotation in G and m_x the mirror reflection $x \rightarrow -x$.

	Construction	Type	Number
structural	$G \in \{C_n, D_n n = 1, 2, 3, 4, 6\}$	monochromatic	10
add \mathcal{T}	$G + G\mathcal{T}$	\mathcal{T} gray	10
add \mathcal{Z}	$G + G\mathcal{Z}$	\mathcal{Z} gray	10
add Ω	$G + G\Omega$	monochromatic	10
add all three	$G + G\mathcal{T} + G\mathcal{Z} + G\Omega$	\mathcal{T}, \mathcal{Z} gray	10
\mathcal{T} dichromatic	$H + (G \setminus H)\mathcal{T}$	\mathcal{T} dichromatic	11
\mathcal{Z} dichromatic	$H + (G \setminus H)\mathcal{Z}$	\mathcal{Z} dichromatic	11
Ω pseudo-dichromatic	$H + (G \setminus H)\Omega$	monochromatic	11
(pseudo-)dichromatic, add \mathcal{T}	$H + (G \setminus H)\mathcal{Z} + [H + (G \setminus H)\mathcal{Z}]\mathcal{T}$	\mathcal{T} gray	11
(pseudo-)dichromatic, add \mathcal{Z}	$H + (G \setminus H)\mathcal{T} + [H + (G \setminus H)\mathcal{T}]\mathcal{Z}$	\mathcal{Z} gray	11
dichromatic, add Ω	$H + (G \setminus H)\mathcal{T} + [H + (G \setminus H)\mathcal{T}]\Omega$	\mathcal{T}, \mathcal{Z} gray	11
double dichromatic with $c_n\mathcal{T}$	$Q + Qc_n\mathcal{T} + Qm_x\Omega + Qc_nm_x\mathcal{Z}$	\mathcal{T}, \mathcal{Z} dichromatic	3
double dichromatic with $c_n\mathcal{Z}$	$Q + Qc_n\mathcal{Z} + Qm_x\Omega + Qc_nm_x\mathcal{T}$	\mathcal{T}, \mathcal{Z} dichromatic	3
double dichromatic with $c_n\Omega$	$Q + Qc_n\Omega + Qm_x\mathcal{T} + Qc_nm_x\mathcal{Z}$	\mathcal{T}, \mathcal{Z} dichromatic	3
			125

by 90°. This reduces the symmetry of the slab to the point group $2/m$ (see Fig. 2). Describing this point group within the coordinate system defined by the slab / CBED experiment (i.e., z -axis parallel to beam slab normal / beam direction), the mirror symmetry along c becomes a mirror along y and the twofold rotation around c becomes a z -reversal combined with a x -mirror. Hence, the twofold rotation is mapped to m_R . Noting that the product of m and m_R is a two-fold rotation within the plane multiplied by z -reversal, i.e. 2_R , the magnetic CBED group of the $[2\bar{1}0]$ slab turns out to be 2_Rmm_R .

These examples illustrate the general procedure we apply to generate the complete mapping of all magnetic point groups: First, we generate a representative magnetic structure for a certain magnetic point group. In the second step, we analyze the preserved symmetry operations for a certain slab orientation. Finally, we map the reversal of the coordinate normal to the slab to the antiunitary z -reversal. To cover all possibilities, i.e., all symmetry classes of slab orientations, we probe all classes of orientations that yield different conventional CBED symmetries, as tabulated in the literature [12]. It turns out that all possible 125 magnetic CBED groups from Sec. III are generated by applying the above algorithm for all 122 three-dimensional magnetic point groups. The above procedure was carried out with the help of a software package provided by De Graef [38].

In Appendix C, we present the full mapping for all distinct beam directions, categorized along crystal classes.

This mapping may be used to determine which CBED data, e.g., which slab orientations need to be prepared and recorded using CBED, are sufficient to unambiguously reconstruct the magnetic-point-group symmetries of the studied sample, similarly to the well-known procedure for the determination of the structural point group by conventional CBED. In the following section, we discuss exemplary electron scattering simulations corroborating the group-theoretical analysis.

V. COMPUTATIONAL EXAMPLES

High-resolution TEM data as well as electron-diffraction data from magnetic crystal structures can be reliably and quantitatively reproduced by numerical integration of Eq. (1) using a split-operator algorithm, referred to as “multislice” in the TEM literature, as described in [29]. Here, the electrostatic scattering potentials were assembled from parameterized atomic potentials described in [39], including experimental values of the Debye-Waller factors [40, 41] and the related complex absorptive part of the potential employing a temperature of 300 K and an acceleration voltage of 300 kV [42]. The parametrized magnetic vector potentials reported in [43] were used. In order to reduce computation time, we did not simulate the thermal diffuse background due to inelastic phonon or magnon scattering in electron diffraction because that background does not affect the

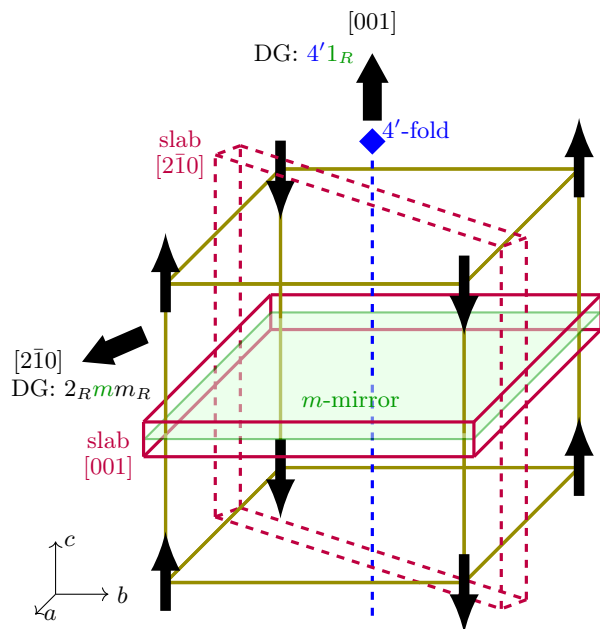


FIG. 2. Magnetic point group $4'/m$ symmetry broken by the slab geometry of a thin TEM sample of tetragonal symmetry. "DG" stands for diffraction group, i.e., magnetic CBED group.

symmetry of elastic CBED patterns. The background is important, however, when considering whether weak magnetic diffraction effects can be reliably measured utilizing a certain electron dose in the experiment [44]. In all simulations, the starting wave function (i.e., the convergent TEM probe beam) has been normalized in intensity to unity when summed over all sampling points of the diffraction pattern. For the exemplary simulations we picked two antiferromagnetic crystals that are suited to illustrate the different aspects of the proposed method.

A. LaMnAsO

The first computational example is LaMnAsO, which is an antiferromagnet with magnetic space group $P4'/n'm'm$ and lattice parameters $a = b = 4.114 \text{ \AA}$ and $c = 9.0304 \text{ \AA}$ [45]. The magnetic moments of Mn atoms are oriented along the easy axis c and are arranged in the antiferromagnetic pattern shown in Fig. 3 [45]. The symmetries of LaMnAsO that are probed by magnetic CBED are described by the point group $4'm'm$. We furthermore note that the point group $4'm'm$ is equivalent to $4'mm'$ obtained by rotating the unit cell through 45° about $[001]$. The latter conventions have been used for the magnetic CBED groups and their mappings to magnetic point groups in Table XI.

Studying Table XI, zone axis orientation $[110]$, corresponding to $[100]$ for the unit-cell convention used in the simulation, is indeed sufficient to uniquely distinguish between the magnetic point-group symmetries compati-

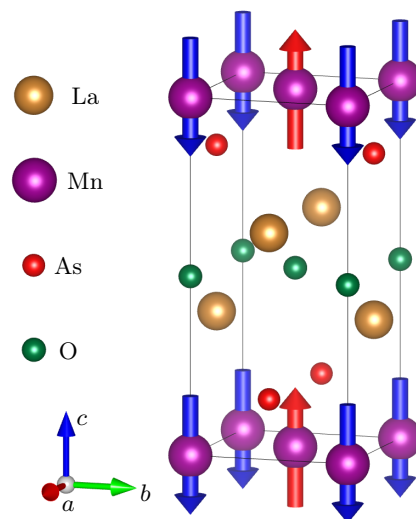


FIG. 3. Crystal structure of LaMnAsO with directions of the Mn magnetic moments.

ble with the structural tetragonal $4mm$ symmetry. We have therefore conducted CBED scattering simulations on slabs oriented along the $[100]$ zones axis. To avoid overlap of the CBED disks at an acceleration voltage of 300 kV, we have chosen a convergence semiangle (i.e., semiangle subtended by converged electron beam) of 1 mrad that is smaller than half the distance between reciprocal lattice points. In order to observe a sufficient level of detail within the Bragg disks, we needed to construct supercells of large lateral size. In the case of $[100]$ zone axis, we have built a supercell of dimensions $31c \times 68a$, which is approximately $28 \text{ nm} \times 28 \text{ nm}$, with a grid of 5580×5576 pixels. The maximal sample thickness was set to $243a$, which is approximately 100 nm.

In total, six multislice calculations have been carried out. Two were non-magnetic (i.e., magnetic vector potential neglected), one for the original structure model (first row in Fig. 4) and the other for a z -reversed structure model (second row) to corroborate the well-known structural symmetry map, which is also included in Table XI as structural point groups. Furthermore, four magnetic calculations have been performed for: (third row) the original structure model (fourth row) with reversed magnetic moments (i.e., time-reversed situation), (fifth row) the z -reversed structure with (sixth row) reversed magnetic moments. Here, it is worth mentioning that magnetic-moment components that are perpendicular (parallel) to the z -axis need to be reversed (stay constant) under z -reversal because the magnetic moments are axial vectors.

The simulated CBED patterns pertaining to the non-magnetic and the magnetic CBED simulations are displayed in the first and third panel of the left column of Fig. 4, respectively. Their intensity is displayed as gray scale. The difference between the non-magnetic and magnetic simulation is visually not noticeable as it

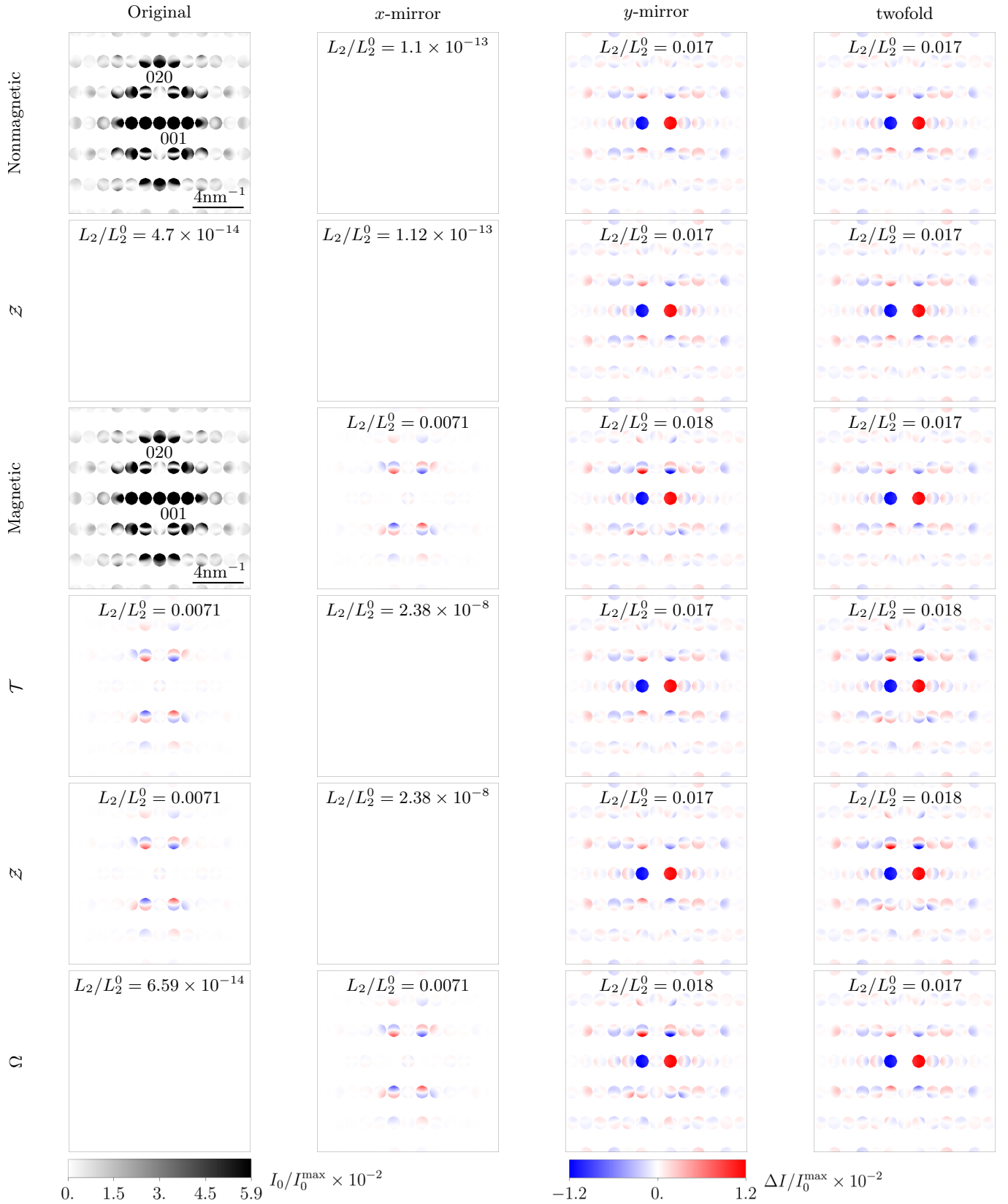


FIG. 4. CBED patterns pertaining to a LaMnAsO slab (thickness ≈ 100 nm) in [100] orientation. Reference non-magnetic and magnetic CBED patterns are shown at beginning of first and third row. Otherwise, differences of CBED patterns are depicted. Rows indicate (1) non-magnetic, (2) z -reversed non-magnetic, (3) magnetic, (4) time- (magnetization-) reversed magnetic, (5) z -reversed magnetic, (6) time- and z -reversed magnetic structure. Columns indicate (1) as computed, (2) x -mirrored, (3) y -mirrored, and (4) 180°-rotated CBED patterns, see text.

amounts to relative intensity variations of the order of 10^{-2} to 10^{-3} , corroborating the weak magnitude of magnetic scattering effects. The CBED patterns exhibit the typical inner structure of the Bragg disks imprinted by dynamical (multiple) scattering. We note, however, that due to the limited sampling of directions in the simulations as well as the saturation of inner Bragg disks in the chosen color scale not all fine details are visible.

Whether a particular symmetry is present in the computed CBED patterns was then checked by computing the difference $\Delta I = I - I_0$ between the CBED pattern obtained by applying the corresponding symmetry transformation and the original one. These difference patterns are displayed in Fig. 4 using a red-blue color scale. Additionally we also provide the Euclidean L_2 norm of ΔI normalized by Euclidean norm of I_0 . Inspecting the non-magnetic results in the first and second row of Fig. 4, we see that the structural CBED symmetries contain x -mirror reflection and z reversal, denoted by $m1_R$, which is predicted by Table XI for the point group $4mm$. Other symmetry operations possible in tetragonal systems, such as a twofold rotation, produce a difference in the percent range and can hence be ruled out.

Turning to the magnetic simulations (third to sixth rows), we observe $m'1'_R$ magnetic CBED symmetry, which again agrees with our predictions, see Table XI. The violation of both m and 1_R symmetries, present in the structural simulation, is only slightly weaker compared to structurally absent symmetries of the third and fourth column. The magnitude of symmetry preservation or violation due to magnetic scattering effects therefore should be accessible in the experiment. Note, however, that signal-to-noise ratios (SNR) and hence CBED acquisition times must be chosen to overcome the large noise background of structural Bragg disks, as discussed in Sec. VI. A partial remedy to the SNR issue is naturally provided by antiferromagnetic materials that possess a magnetic unit cell that is larger (typically by a factor of 2) than the structural one. This class of antiferromagnets exhibit purely magnetic Bragg reflections without a structural contribution and thus a significantly larger SNR in these discs. In the next subsection, we will discuss a prominent member of this family, antiferromagnetic NiO.

B. NiO

NiO is a Mott-insulating antiferromagnet below a Néel temperature of 523 K [46]. Its paramagnetic phase has cubic $Fm\bar{3}m$ symmetry with lattice constant $a = 4.17 \text{ \AA}$, which becomes monoclinic C_22/c (BNS magnetic space group notation [47]) in the antiferromagnetic phase [48] (Fig. 5). The latter involves a doubling of the magnetic unit cell. The monoclinic axis of the magnetic unit cell points into the $[1\bar{1}0]_c$ direction (the cubic notation is indicated by the subscript c) and the spins are oriented along the easy axis $[11\bar{2}]_c$, which is perpendicular to the

monoclinic axis. It is also important to note that NiO undergoes a spin-flop transition at an external magnetic field of 1.54 T, where spins reorient perpendicular to the field direction [49]. Indeed, Loudon [22] detected the purely magnetic reflections of the spin-flopped phase by conventional broad-beam electron diffraction, where the objective lens typically imposes external fields well above the spin-flop field. The magnetic symmetry of the spin-flopped phase has not been reported yet.

We performed two sets of simulations, one for the original phase and one for the spin-flopped phase. The slab orientation for the original phase was the monoclinic axis $[1\bar{1}0]_c$. The slab orientation for the spin-flopped phase was $[11\bar{2}]_c$, corresponding to the monoclinic a -axis, and the spin orientation in the spin-flopped phase was along $[1\bar{1}0]_c$ (monoclinic b -axis). The slab thickness was set to approximately 102 nm. Again, we conducted four magnetic CBED simulations, covering all possible combinations of z and time reversal.

In contrast to LaMnAsO, we can now directly read off the symmetries from the purely magnetic reflections displayed in Figs. 6 and 7. Here, in order to display their internal structure, a gray scale was chosen that saturates the structural Bragg disks. The CBED pattern of the original phase exhibits twofold rotational symmetry as well as both z -reversal and time-reversal symmetries, i.e., $21_R1'$ in total, see Fig. 6. Inspecting Table VIII, this symmetry corresponds to the gray point group $2/m1'$, which corresponds to the magnetic point group symmetries obtained by stripping all translations from the NiO space group C_22/c . Indeed, the glide plane translation along the monoclinic c direction does not break the symmetry for the slab oriented along monoclinic b -axis since c is perpendicular to b , and leaves the slab invariant. Consequently, the glide plane symmetry translates into a simple mirror symmetry denoted by $/m$ in the $2/m1'$ diffraction group mentioned above. Similarly, the $1'_c$ symmetry (abbreviated by the subscript c attached to C centering in the space group symbol), i.e., the combination of time reversal and in-plane translation along c corresponds to a simple time reversal symmetry $1'$ since the translation leaves the slab invariant.

In the spin-flopped case, each CBED pattern exhibits a mirror (m) symmetry with respect to the x axis, see Fig. 7. Moreover, an m_R symmetry is discernible by comparing the z -reversed CBED patterns in the upper and lower row of Fig. 7. Similarly, we can verify the presence of a 2_R rotational symmetry. Further symmetries including those involving time reversal are absent. Consequently, the CBED symmetry observed in this orientation is 2_Rmm_R , which can be associated uniquely to the monoclinic magnetic point group $2/m$. Indeed, inspecting the magnetic unit cell, we observe that the space group symmetry of the spin-flopped phase is C_22/m , which contains the point group transformations $2/m$. The combined translation and time-reversal symmetry $1'_c$ (again abbreviated by the c index in the space group notation) is broken in the a -oriented slab because the a

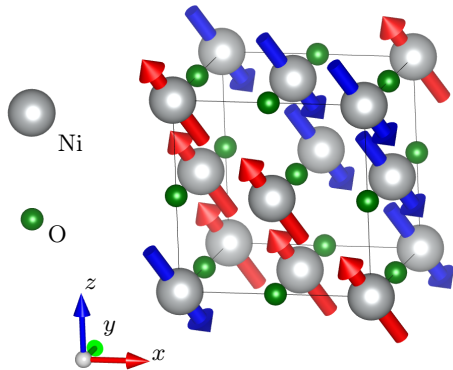


FIG. 5. Crystal structure of NiO with directions of the magnetic moments. Note that only one structural cubic unit cell is displayed. The cubic antiferromagnetic unit cell is twice as large in each direction. The magnetic monoclinic unit cell, on the other hand, lies askew within the cubic cell and has the same volume.

and c axes are not perpendicular, i.e., the c translation is not in plane.

VI. EXPERIMENTAL CHALLENGES

Having established the theoretical framework for the determination of magnetic point-group symmetries from CBED patterns, we briefly discuss possible experimental realizations. We expect five main challenges to play a crucial role:

1. We observed that the modifications of CBED patterns due to magnetic scattering is quite small for antiferromagnets. Overall relative intensity changes (L_2 norm) to be detected are on the order of 0.1% with local relative changes in intensity reaching 1% with respect to structural reflections. Consequently, the challenge is to measure a small signal on top of a strong signal with corresponding noise level. To measure the weak signal above that background noise level, one should employ low-noise detectors of high dynamic range (e.g., hybrid pixel detectors) and long acquisition times. If studying antiferromagnets with a doubled magnetic unit cell that give rise to purely magnetic Bragg reflections, e.g., NiO, one may focus on these reflections, which do not suffer from a strong structural background signal.
2. For the determination of magnetic symmetries, the experimental realization of magnetization (time) reversal without changing the structure is crucial. There are several possibilities, depending on the particular magnetic material to be studied. One can briefly heat up the sample above its Néel or Curie temperature. If there is no bias for one orientation this would allow magnetization reversal in

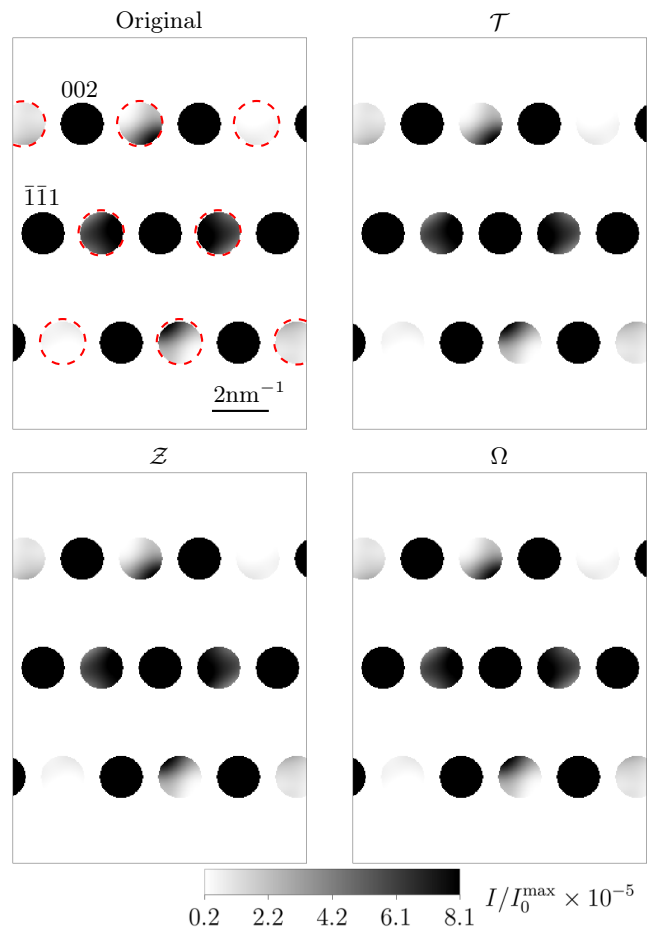


FIG. 6. CBED patterns pertaining to the magnetic ground state NiO slab in $[1\bar{1}0]_c$ orientation. Purely magnetic reflections are indicated by dashed red circles.

a randomized way. Similarly, short application of an external field may trigger a spin flop for antiferromagnets, after which a random magnetization reversal may occur if no bias is present. Finally, one may trigger the movement of domain walls by applying external fields [50] and thereby change the magnetic domain orientation in the observed area.

3. Standard CBED and other diffraction experiments in the transmission electron microscope are carried out with the sample immersed within the strong magnetic field of the objective lens of up to 2.5 T, which permits very short camera lengths and hence recording of large CBED patterns without significant aberrations. If the influence of the magnetic field from the objective lens is not desired, e.g., because it triggers an unwanted spin-flop transition, a zero-field experiment adaption of CBED is required. This may require additional instrumental modifications of the transmission electron microscope, e.g., a zero-field objective lens or a Lorentz lens.

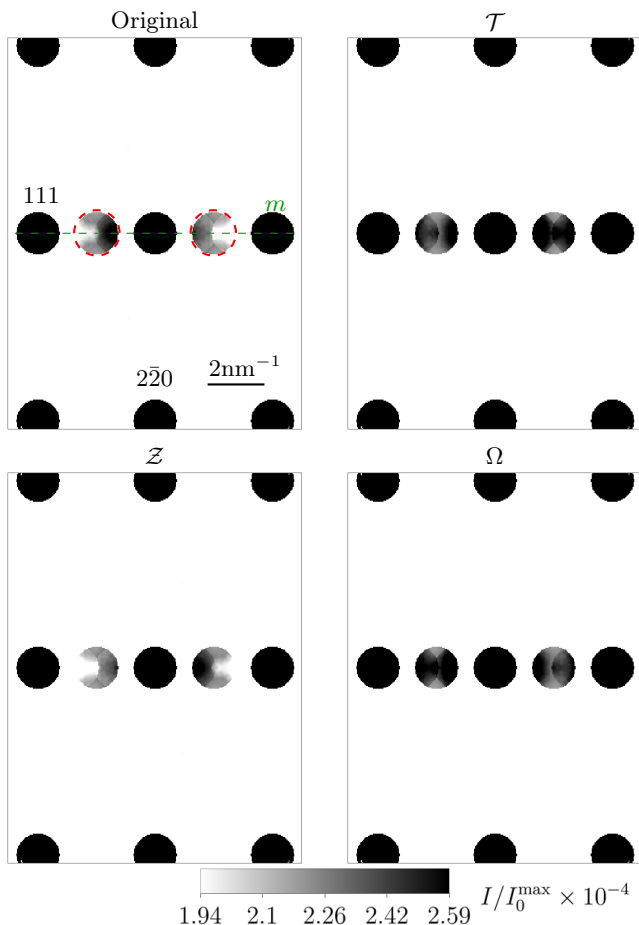


FIG. 7. CBED patterns pertaining to the spin-flopped NiO slab in $[11\bar{2}]_c$ orientation. The spin orientation is $[1\bar{1}0]_c$. Purely magnetic reflections are indicated by dashed red circles.

4. The z -reversal symmetries are generally difficult to observe experimentally because the experimentally prepared crystal slab is breaking these symmetries when the upper and lower crystal plane are not identical. As a result, probing z -reversal symmetries may be unfeasible. An unambiguous determination of point-group symmetries would then require probing additional slab orientations.
5. The proposed magnetic CBED can only provide magnetic point-group symmetries. The point-group transformations being part of glide-plane and screw-axis symmetries are typically not visible, except for some special slab orientations, where the corresponding translations are within the slab plane (see above example of spin-flopped NiO). Consequently, the detection of space-group symmetries requires additional care and may involve more sophisticated methods such as inspection of kinematically forbidden reflections or higher-order Laue zones, similar to conventional CBED [51].

VII. SUMMARY

In this work, we have introduced magnetic CBED for the unambiguous determination of magnetic-point-group symmetries. We have classified all magnetic point-group symmetries of the diffraction patterns in terms of 125 magnetic CBED groups. The subsequent mapping of all magnetic point groups to corresponding magnetic CBED groups allows the determination of the latter from a finite series of CBED experiments at different crystal orientations. The signal level required for a successful experimental realization of the proposed method is, in principle, achievable in modern transmission electron microscopes. Simplicity, accuracy, cost-effectiveness, and very small required sample sizes, down to about 50 nm, make magnetic CBED an intriguing alternative to neutron diffraction for magnetic-symmetry detection, e.g., for the large class of magnetic micro- and nanoparticles, polycrystalline magnetic matter, magnetic thin films, and magnetic van der Waals materials. Moreover, the high-spatial resolution, down to about 10 nm, in principle facilitates mapping of symmetries, e.g., across phase and domain boundaries, by recording magnetic CBED patterns at different positions. We therefore foresee manifold applications for magnetic CBED as a symmetry probe for magnetic crystalline matter.

VIII. ACKNOWLEDGEMENTS

The authors are grateful to Juri Barthel for useful discussions. Financial support by the Deutsche Forschungsgemeinschaft through Collaborative Research Center SFB 1143, projects A04 and C04, project id 247310070, and the Würzburg–Dresden Cluster of Excellence ct.qmat, EXC 2147, project id 390858490, is gratefully acknowledged. J. R. and J.-Á. C.-R. acknowledge the support of the Swedish Research Council (grant no. 2021-03848), the Olle Engkvist’s Foundation (grant no. 214-0331), and the Knut and Alice Wallenberg Foundation (grant no. 2022.0079). The simulations were enabled by resources provided by the National Academic Infrastructure for Supercomputing in Sweden (NAISS) at the NSC Centre, partially funded by the Swedish Research Council through grant agreement no. 2022-06725.

Appendix A: Detailed derivation of the paraxial scattering equation

Since the effects of the electron spin, such as spin-orbit coupling and Zeeman coupling, are negligible for small-angle scattering of high-energy beam electrons their energy eigenstates are well described by a stationary Klein-Gordon equation, minimally coupled to static electric and magnetic potentials (arguments have been omitted),

$$(E + e\Phi)^2 \psi = \left(c^2 (-i\hbar\nabla + e\mathbf{A})^2 + m_e^2 c^4 \right) \psi. \quad (\text{A1})$$

Because of to high energy E of highly accelerated electrons in a Transmission Electron Microscope the electric potential squared term can be neglected, which is referred to as the high-energy approximation [52]. After a couple of rearrangements and dividing by $E = \gamma m_e c^2$, where $\gamma = 1/\sqrt{1 - v^2/c^2}$ is the Lorentz factor, this high-energy limit of the Klein-Gordon equation takes a form that is mathematically equivalent to the stationary Schrödinger equation [28]

$$\frac{\gamma^2 - 1}{2\gamma} m_e c^2 \psi = \frac{1}{2\gamma m_e} (-i\hbar\nabla + e\mathbf{A})^2 \psi - e\Phi\psi. \quad (\text{A2})$$

As a consequence of the high kinetic energy of the beam electrons, typical targets (samples) brought into their path do not deflect the electrons by large angles. This observation motivates the paraxial approximation, where the wave is separated into a fast plane wave and a slowly varying envelope function in the propagation direction z ,

$$\psi(\mathbf{r}_\perp, z) = \Psi(\mathbf{r}_\perp, z) e^{ik_0 z}, \quad (\text{A3})$$

where \mathbf{r}_\perp denotes the two-dimensional coordinates in the xy plane and $k_0 = \gamma m_e v/\hbar$ the wave number of the fast carrier wave. Upon insertion of this ansatz into Eq. (A2), one can neglect the second-order derivative of the slowly varying envelope function with respect to z as well as first-order derivatives with respect to z multiplied with the small A_z . Both approximations are motivated by the large k_0 . Moreover, A_z^2 can safely be dropped for the same reason. One finally obtains the paraxial Schrödinger equation

$$i \frac{\partial \Psi}{\partial z} = \left(\frac{1}{2k_0} \left(-i\nabla_\perp + \frac{e}{\hbar} \mathbf{A}_\perp \right)^2 + \frac{e}{\hbar} A_z - \frac{e}{\hbar v} \Phi \right) \Psi. \quad (\text{A4})$$

Appendix B: Details of the construction of magnetic diffraction groups

In this Appendix, we explain the construction of magnetic CBED groups in detail. As noted in Sec. III, 10 possible structural point groups exist for a slab. These groups do not contain any antiunitary elements and are called monochromatic. In addition, the magnetic CBED groups can contain the antiunitary time-reversal operation \mathcal{T} , the antiunitary z reversal \mathcal{Z} , or their unitary product Ω , each either as a new generator or multiplying all elements of the coset $G \setminus H$ of a halving subgroup H of the structural group G .

Let G denote any of the structural point groups C_n and D_n with $n = 1, 2, 3, 4, 6$, where we use the standard Schoenflies notation for two-dimensional point groups (rosette groups). Adding \mathcal{T} as a new generator leads to the 10 groups $G + G\mathcal{T}$, which we now call “ \mathcal{T} gray” to distinguish them from the following class. Instead adding \mathcal{Z} leads to the 10 groups $G + G\mathcal{Z}$, which we call “ \mathcal{Z} gray.” Finally, adding Ω as a new generator leads to the

TABLE II. Structural monochromatic (first and second column), \mathcal{T} gray (third column), and \mathcal{Z} gray (fourth column) CBED groups. The Schoenflies notation is given for the monochromatic groups. The Hermann–Mauguin notation [53] is presented for all groups, where $1'$ refers to the time-reversal operation \mathcal{T} and 1_R denotes the z -reversal operation \mathcal{Z} .

Monochromatic groups	\mathcal{T} gray groups	\mathcal{Z} gray groups	
C_1	1	$11'$	11_R
C_2	2	$21'$	21_R
C_3	3	$31'$	31_R
C_4	4	$41'$	41_R
C_6	6	$61'$	61_R
D_1	m	$m1'$	$m1_R$
D_2	$2mm$	$2mm1'$	$2mm1_R$
D_3	$3m$	$3m1'$	$3m1_R$
D_4	$4mm$	$4mm1'$	$4mm1_R$
D_6	$6mm$	$6mm1'$	$6mm1_R$

TABLE III. Monochromatic CBED groups containing the product $\Omega = \mathcal{T}\mathcal{Z}$ of time and z reversal (first column) and CBED groups that are both \mathcal{T} gray and \mathcal{Z} gray (second column). The Hermann–Mauguin notation [53] is presented for all groups. 1_R denotes the product operation Ω . Note that $1'_R$ is not given explicitly for the \mathcal{T} and \mathcal{Z} gray groups since it is generated by $1'$ and 1_R .

Monochromatic groups with Ω	\mathcal{T} and \mathcal{Z} gray groups
$11'_R$	$11'1_R$
$21'_R$	$21'1_R$
$31'_R$	$31'1_R$
$41'_R$	$41'1_R$
$61'_R$	$61'1_R$
$m1'_R$	$m1'1_R$
$2mm1'_R$	$2mm1'1_R$
$3m1'_R$	$3m1'1_R$
$4mm1'_R$	$4mm1'1_R$
$6mm1'_R$	$6mm1'1_R$

10 groups $G + G\Omega$. These groups only contain unitary elements and are thus monochromatic. We can also add two of \mathcal{T} , \mathcal{Z} , or Ω as new generators. Since the product of any two of these is the third, this only produces 10 additional groups $G + G\mathcal{T} + G\mathcal{Z} + G\Omega$. These groups are both \mathcal{T} gray and \mathcal{Z} gray. The groups constructed so far are listed in Tables II and III.

Moreover, for any structural group G that has a halving subgroup H , the elements of the coset $G \setminus H$ can

TABLE IV. Dichromatic CBED groups based on time reversal \mathcal{T} (first and second column). The Schoenflies notation $G(H)$ for the group $H + (G \setminus H)\mathcal{T}$ and the Hermann–Mauguin notation [53] are given. The third and fourth column show the \mathcal{Z} dichromatic CBED groups and the “pseudo-dichromatic” (but actually monochromatic) CBED groups based on Ω . In the Hermann–Mauguin notation, a prime means that the corresponding generator is multiplied by the time-reversal operation \mathcal{T} , a subscript “ R ” denotes multiplication by \mathcal{Z} , and a prime combined with a subscript “ R ” denotes multiplication by Ω .

\mathcal{T} dichromatic groups	\mathcal{Z} dichromatic groups	Pseudo-dichromatic groups
$C_2(C_1)$	$2'$	2_R
$C_4(C_2)$	$4'$	4_R
$C_6(C_3)$	$6'$	6_R
$D_1(C_1)$	m'	m_R
$D_2(D_1)$	$2'mm'$	2_Rmm_R
$D_2(C_2)$	$2m'm'$	$2m_Rm_R$
$D_3(C_3)$	$3m'$	$3m_R$
$D_4(D_2)$	$4'mm'$	4_Rmm_R
$D_4(C_4)$	$4m'm'$	$4m_Rm_R$
$D_6(D_3)$	$6'mm'$	6_Rmm_R
$D_6(C_6)$	$6m'm'$	$6m_Rm_R$

be multiplied by \mathcal{T} , \mathcal{Z} , or Ω . For time reversal \mathcal{T} , this leads to the standard dichromatic groups $H + (G \setminus H)\mathcal{T}$, of which there are 11. These are listed in Table IV. As shown in this table, the allowed structural groups have zero, one, or two halving subgroups. Performing the same operation with the z reversal operation \mathcal{Z} , we obtain another 11 dichromatic groups $H + (G \setminus H)\mathcal{Z}$. Finally, using Ω , we obtain 11 groups $H + (G \setminus H)\Omega$, which are monochromatic since Ω is unitary but could be called “pseudo-dichromatic” to highlight their structure. All these groups are also included in Table IV.

Interestingly, dichromatic groups with respect to \mathcal{T} are automatically also dichromatic with respect to \mathcal{Z} and vice versa. To see this, consider a \mathcal{T} dichromatic group $M = H + (G \setminus H)\mathcal{T}$. Define another group

$$\tilde{G} \equiv H + (G \setminus H)\Omega. \quad (\text{B1})$$

H is a halving subgroup of \tilde{G} . Now we construct the \mathcal{Z} dichromatic group based on \tilde{G} and H :

$$\begin{aligned} \tilde{M} &= H + (\tilde{G} \setminus H)\mathcal{Z} = H + (G \setminus H)\Omega\mathcal{Z} \\ &= H + (G \setminus H)\mathcal{T} = M. \end{aligned} \quad (\text{B2})$$

Thus the same group can be understood as \mathcal{T} dichromatic or as \mathcal{Z} dichromatic, though based on different monochromatic groups G and \tilde{G} , respectively. However,

the \mathcal{Z} dichromatic groups in Tables I and IV are nevertheless distinct from the \mathcal{T} dichromatic groups since the groups \tilde{G} are not one of the structural point groups in all these cases.

Further groups can be constructed by taking a group that is dichromatic with respect to \mathcal{T} or \mathcal{Z} or pseudo-dichromatic with respect to Ω and add one generator. If it is the same element we do not obtain new groups:

$$\begin{aligned} M &= H + (G \setminus H)A + [H + (G \setminus H)A]A \\ &= H + G \setminus H + HA + (G \setminus H)A \\ &= G + GA, \end{aligned} \quad (\text{B3})$$

where $A \in \{\mathcal{T}, \mathcal{Z}, \Omega\}$. If it is a different generator we instead find

$$\begin{aligned} M &= H + (G \setminus H)A + [H + (G \setminus H)A]B \\ &= H + HB + (G \setminus H)C + (G \setminus H)BC \\ &= H + (G \setminus H)C + [H + (G \setminus H)C]B, \end{aligned} \quad (\text{B4})$$

where $A, B \in \{\mathcal{T}, \mathcal{Z}, \Omega\}$ and $AB = C \in \{\mathcal{T}, \mathcal{Z}, \Omega\}$. We see that A and C can be interchanged without generating a new group. Furthermore, choosing B fixes the A and C up to their irrelevant order since A , B , and C are distinct by construction. Hence, for each structural group G and subgroup H , there are three new groups distinguished by the choice of B . These groups can be written as (the two forms corresponding to the interchange of A and C are both given in all three cases)

$$\begin{aligned} H + (G \setminus H)\mathcal{Z} + [H + (G \setminus H)\mathcal{Z}]\mathcal{T} \\ = H + (G \setminus H)\Omega + [H + (G \setminus H)\Omega]\mathcal{T}, \end{aligned} \quad (\text{B5})$$

$$\begin{aligned} H + (G \setminus H)\mathcal{T} + [H + (G \setminus H)\mathcal{T}]\mathcal{Z} \\ = H + (G \setminus H)\Omega + [H + (G \setminus H)\Omega]\mathcal{Z}, \end{aligned} \quad (\text{B6})$$

$$\begin{aligned} H + (G \setminus H)\mathcal{T} + [H + (G \setminus H)\mathcal{T}]\Omega \\ = H + (G \setminus H)\mathcal{Z} + [H + (G \setminus H)\mathcal{Z}]\Omega \\ = H + H\Omega + [G \setminus H + (G \setminus H)\Omega]\mathcal{T} \\ = H + H\Omega + [G \setminus H + (G \setminus H)\Omega]\mathcal{Z}. \end{aligned} \quad (\text{B7})$$

The first class is obviously \mathcal{T} gray, the second is \mathcal{Z} gray, and the third is both. These 33 new groups are listed in Table V. If we instead start from a dichromatic or pseudo-dichromatic group and add any two of \mathcal{T} , \mathcal{Z} , or Ω , the third element is also an element of the group. This does not produce a new group since

$$\begin{aligned} M &= H + (G \setminus H)A + [H + (G \setminus H)A]\mathcal{T} \\ &\quad + [H + (G \setminus H)A]\mathcal{Z} + [H + (G \setminus H)A]\Omega \\ &= G + G\mathcal{T} + G\mathcal{Z} + G\Omega, \end{aligned} \quad (\text{B8})$$

where $A \in \{\mathcal{T}, \mathcal{Z}, \Omega\}$.

The final class of magnetic CBED groups emerges if one multiplies the coset $G \setminus H_1$ for a halving subgroup H_1 by $A \in \{\mathcal{T}, \mathcal{Z}, \Omega\}$ and the coset $G \setminus H_2$ for another halving subgroup H_2 by $B \in \{\mathcal{T}, \mathcal{Z}, \Omega\}$. If H_1 and H_2 are equal one does not obtain new groups because each

TABLE V. Mixed (pseudo-)dichromatic and gray CBED groups. See Eqs. (B5)–(B7) for the construction scheme based on the structural groups.

\mathcal{T} gray groups	\mathcal{Z} gray groups	\mathcal{T} and \mathcal{Z} gray groups
$2_R 1'$	$2' 1_R$	$2' 1'_R$
$4_R 1'$	$4' 1_R$	$4' 1'_R$
$6_R 1'$	$6' 1_R$	$6' 1'_R$
$m_R 1'$	$m' 1_R$	$m' 1'_R$
$2_R m m_R 1'$	$2' m m' 1_R$	$2' m m' 1'_R$
$2 m_R m_R 1'$	$2 m' m' 1_R$	$2 m' m' 1'_R$
$3 m_R 1'$	$3 m' 1_R$	$3 m' 1'_R$
$4_R m m_R 1'$	$4' m m' 1_R$	$4' m m' 1'_R$
$4 m_R m_R 1'$	$4 m' m' 1_R$	$4 m' m' 1'_R$
$6_R m m_R 1'$	$6' m m' 1_R$	$6' m m' 1'_R$
$6 m_R m_R 1'$	$6 m' m' 1_R$	$6 m' m' 1'_R$

of the operations \mathcal{T} , \mathcal{Z} , and Ω squares to the identity and the product of any two of them is the third.

Hence, we require the structural point group G to have two distinct halving subgroups. This applies to three of the relevant groups: $D_2 = 2mm$, $D_4 = 4mm$, and $D_6 = 6mm$, which each have exactly two distinct halving subgroups. In all three cases, the intersection of the two subgroups H_1 and H_2 is a halving subgroup of both H_1 and H_2 and is thus a quartering subgroup of G . We denote this subgroup by $Q = H_1 \cap H_2$. The only quartering subgroups that appear are C_1 , C_2 , and C_3 .

Let h_1 be a generator of H_1 that is not an element of H_2 and let h_2 be a generator of H_2 that is not an element of H_1 . Hence, h_1 and h_2 are not elements of Q . Then G can be decomposed into cosets according to

$$\begin{aligned} G &= Q + Qh_1 + Qh_2 + Qh_1h_2 \\ &= Q + Qh_1 + Qh_2 + Qh_2h_1. \end{aligned} \quad (\text{B9})$$

The last equality also holds if h_1 and h_2 do not commute since Qh_2h_1 is just a reordering of Qh_1h_2 . Moreover, we find

$$Qh_1 + Qh_2h_1 = H_2h_1 = G \setminus H_2, \quad (\text{B10})$$

$$Qh_2 + Qh_1h_2 = H_1h_2 = G \setminus H_1. \quad (\text{B11})$$

By multiplying these complements by *the same* element $A \in \{\mathcal{T}, \mathcal{Z}, \Omega\}$, we do not obtain new groups since

$$\begin{aligned} M &= Q + Qh_1A + Qh_2A + Qh_1h_2A^2 \\ &= Q + Qh_1h_2 + (Qh_1 + Qh_2)A \\ &= Q + Qh_1h_2 + [G \setminus (Q + Qh_1h_2)]A \end{aligned} \quad (\text{B12})$$

is a dichromatic or pseudo-dichromatic group already contained in Table IV.

TABLE VI. Double dichromatic CBED groups. The construction scheme is discussed in the text.

Double dichromatic groups		
$2' m'_R m_R$	$2_R m'_R m'$	$2'_R m' m_R$
$4' m'_R m_R$	$4_R m'_R m'$	$4'_R m' m_R$
$6' m'_R m_R$	$6_R m'_R m'$	$6'_R m' m_R$

By instead multiplying the complements by distinct elements $A, B \in \{\mathcal{T}, \mathcal{Z}, \Omega\}$, we obtain the groups

$$M = Q + Qh_1A + Qh_2B + Qh_1h_2C, \quad (\text{B13})$$

where $C = AB \in \{\mathcal{T}, \mathcal{Z}, \Omega\}$. Interchanging h_1 and h_2 has the same effect as interchanging A and B . Here, we fix h_1 and h_2 and consider all choices for A and B . Specifically, we choose h_1 to be the generator c_n , $n = 2, 4, 6$, of rotations (we use lower-case “ c ” to avoid confusion with the groups C_n) and h_2 as the mirror reflection m_x , choosing the x -axis normal to the mirror plane. The resulting groups are

$$M = Q + Qc_nA + Qm_xB + Qc_nm_xC, \quad (\text{B14})$$

where Q is one of the groups C_1 , C_2 , and C_3 . The explicit groups M are

$$\text{from } D_2: \{1, c_2A, m_xB, m_yC\}, \quad (\text{B15})$$

$$\begin{aligned} \text{from } D_4: \{1, c_4A, c_2, c_4^{-1}A, \\ m_xB, c_4m_xC, c_2m_xB, c_4^{-1}m_xC\}, \end{aligned} \quad (\text{B16})$$

$$\begin{aligned} \text{from } D_6: \{1, c_6A, c_3, c_2A, c_3^{-1}, c_6^{-1}A, m_xB, c_6m_xC, \\ c_3m_xB, c_2m_xC, c_3^{-1}m_xB, c_6^{-1}m_xC\}. \end{aligned} \quad (\text{B17})$$

We see that by a suitable rotation about the z -axis, B and C are interchanged. This rotation is not considered to lead to a distinct group. The three choices for A together with the three choices of the structural group D_2 , D_4 , and D_6 (or of the quartering group C_1 , C_2 , and C_3) generate nine new groups, which are listed in Table VI. These groups are dichromatic since half of the elements are antiunitary. We call them “double dichromatic” because they are dichromatic with respect to both \mathcal{T} and \mathcal{Z} involving distinct decompositions of the structural group.

Appendix C: Mappings of magnetic point groups to magnetic CBED groups

In this Appendix, we list the mapping from the 122 three-dimensional magnetic point groups to the 125 magnetic CBED groups for all distinct beam directions. The tables are organized according to crystal classes: The mappings for triclinic point groups are shown in Table VII, those for monoclinic groups in Table VIII, those for orthorhombic groups in Table IX, those for tetragonal groups in Tables X and XI, those for trigonal groups

TABLE VII. Assignment of triclinic magnetic point groups to magnetic CBED groups.

PG	mPG	mDG for beam directions
		$[uvw]$
1 (C_1)	1	1
1	11'	11'
$\bar{1}$ (C_i)	$\bar{1}$	2_R
$\bar{1}$	$\bar{1}1'$	$2_R1'$
$\bar{1}$	$\bar{1}'$	$2'_R$

TABLE VIII. Assignment of monoclinic magnetic point groups to magnetic CBED groups.

PG	mPG	mDG for beam directions		
		$[010]$	$[u0w]$	$[uvw]$
2 (C_2)	2	2	m_R	1
2	21'	21'	m_R1'	11'
2	2'	2'	m'_R	1
m (C_s)	m	1_R	m	1
m	$m1'$	$1_R1'$	$m1'$	11'
m	m'	$1'_R$	m'	1
$2/m$ (C_{2h})	$2/m$	21_R	2_Rmm_R	2_R
$2/m$	$2/m1'$	$21_R1'$	$2_Rmm_R1'$	$2_R1'$
$2/m$	$2/m'$	$21'_R$	$2'_Rm'm_R$	$2'_R$
$2/m$	$2'/m'$	$2'1'_R$	$2_Rm'm'_R$	2_R
$2/m$	$2'/m$	$2'1_R$	$2'_Rmm'_R$	$2'_R$

in Tables XII and XIII, those for hexagonal groups in Tables XIV and XV, and those for cubic groups in Tables XVI and XVII. In all tables, the mapping of magnetic point groups (mPG) to magnetic CBED groups (magnetic diffraction groups, mDG) is shown for all slab orientations. The underlying structural point group is given in Hermann-Mauguin and, at the first occurrence, also in Schoenflies notation. The slab normal is parallel to the beam direction, which is denoted by $[uvw]$ in crystallographic coordinates. Here, variables u , v , w stand for generic values, which are distinct from the special values given in the tables to denote high-symmetry directions. All tables also show the corresponding structural point group (PG). We note that there are occasional permutations of the symmetry symbols in the point group notations, e.g., $mm2$ instead of $2mm$, corresponding to different choices of unit cell orientations. By using them we follow established conventions in the literature [12, 13]. These permutations do not affect the symmetry considerations.

TABLE IX. Assignment of orthorhombic magnetic point groups to magnetic CBED groups.

PG	mPG	mDG for beam directions						
		[010]	[001]	[100]	[u0w]	[uv0]	[0vw]	[uvw]
222 (D_2)	222	$2m_R m_R$	$2m_R m_R$	$2m_R m_R$	m_R	m_R	m_R	1
222	2221'	$2m_R m_R 1'$	$2m_R m_R 1'$	$2m_R m_R 1'$	$m_R 1'$	$m_R 1'$	$m_R 1'$	11'
222	2'2'2	$2' m_R m'_R$	$2m'_R m'_R$	$2' m_R m'_R$	m'_R	m_R	m'_R	1
$mm2$ (C_{2v})	$mm2$	$m 1_R$	$2mm$	$m 1_R$	m	m_R	m	1
$mm2$	$mm2 1'$	$m 1_R 1'$	$2mm 1'$	$m 1_R 1'$	$m 1'$	$m_R 1'$	$m 1'$	11'
$mm2$	$m' m' 2$	$m' 1'_R$	$2m' m'$	$m' 1'_R$	m'	m_R	m'	1
$mm2$	$m' m' 2'$	$m' 1_R$	$2' m m'$	$m 1'_R$	m	m'_R	m'	1
mmm (D_{2h})	mmm	$2mm 1_R$	$2mm 1_R$	$2mm 1_R$	$2_R m m_R$	$2_R m m_R$	$2_R m m_R$	2_R
mmm	$mmm 1'$	$2mm 1_R 1'$	$2mm 1_R 1'$	$2mm 1_R 1'$	$2_R m m_R 1'$	$2_R m m_R 1'$	$2_R m m_R 1'$	$2_R 1'$
mmm	$m' m' m$	$2' m m' 1'_R$	$2m' m' 1_R$	$2' m m' 1'_R$	$2_R m' m'_R$	$2_R m m_R$	$2_R m' m'_R$	2_R
mmm	$m' m' m'$	$2m' m' 1'_R$	$2m' m' 1'_R$	$2m' m' 1'_R$	$2'_R m' m_R$	$2'_R m' m_R$	$2'_R m' m_R$	$2'_R$
mmm	mmm'	$2' m m' 1_R$	$2mm 1'_R$	$2' m m' 1_R$	$2'_R m m'_R$	$2'_R m' m_R$	$2'_R m m'_R$	$2'_R$

TABLE X. Assignment of tetragonal magnetic point groups to magnetic CBED groups.

PG	mPG	mDG for beam directions		
		[001]	[<i>uv</i> 0]	[<i>uvw</i>]
4 (C_4)	4	4	m_R	1
4	41'	41'	$m_R 1'$	11'
4	4'	4'	m_R	1
$\bar{4}$ (S_4)	$\bar{4}$	4 _R	m_R	1
$\bar{4}$	$\bar{4}1'$	4 _R 1'	$m_R 1'$	11'
$\bar{4}$	$\bar{4}'$	4' _R	m_R	1
4/ <i>m</i> (C_{4h})	4/ <i>m</i>	41 _R	2 _R <i>mm</i> _R	2 _R
4/ <i>m</i>	4/ <i>m</i> 1'	41 _R 1'	2 _R <i>mm</i> _R 1'	2 _R 1'
4/ <i>m</i>	4'/ <i>m</i>	4' _R 1 _R	2 _R <i>mm</i> _R	2 _R
4/ <i>m</i>	4/ <i>m</i> '	41' _R	2' _R <i>m</i> ' _R <i>m</i> _R	2' _R
4/ <i>m</i>	4'/ <i>m</i> '	4' _R 1' _R	2' _R <i>m</i> ' _R <i>m</i> _R	2' _R

TABLE XI. Assignment of tetragonal magnetic point groups to magnetic CBED groups (continued).

PG	mPG	mDG for beam directions						
		[001]	$\langle 100 \rangle$	$\langle 110 \rangle$	$[u0w]$	$[uv0]$	$[uuw]$	$[uvw]$
422 (D_4)	422	$4m_R m_R$	$2m_R m_R$	$2m_R m_R$	m_R	m_R	m_R	1
422	4221'	$4m_R m_R 1'$	$2m_R m_R 1'$	$2m_R m_R 1'$	$m_R 1'$	$m_R 1'$	$m_R 1'$	11'
422	4'22'	$4'm_R m'_R$	$2m_R m_R$	$2'm_R m'_R$	m_R	m_R	m'_R	1
422	42'2'	$4m'_R m'_R$	$2'm_R m'_R$	$2'm_R m'_R$	m'_R	m_R	m'_R	1
4mm (C_{4v})	4mm	4mm	$m1_R$	$m1_R$	m	m_R	m	1
4mm	4mm1'	4mm1'	$m1_R 1'$	$m1_R 1'$	$m1'$	$m_R 1'$	$m1'$	11'
4mm	4'mm'	4'mm'	$m1_R$	$m'1'_R$	m	m_R	m'	1
4mm	4m'm'	4m'm'	$m'1'_R$	$m'1'_R$	m'	m_R	m'	1
$\bar{4}2m$ (D_{2d})	$\bar{4}2m$	$4_R m m_R$	$2m_R m_R$	$m1_R$	m_R	m_R	m	1
$\bar{4}2m$	$\bar{4}2m1'$	$4_R m m_R 1'$	$2m_R m_R 1'$	$m1_R 1'$	$m_R 1'$	$m_R 1'$	$m1'$	11'
$\bar{4}2m$	$\bar{4}'2m'$	$4'_R m' m_R$	$2m_R m_R$	$m'1'_R$	m_R	m_R	m'	1
$\bar{4}2m$	$\bar{4}'2'm$	$4'_R m m'_R$	$2'm_R m'_R$	$m1_R$	m'_R	m_R	m	1
$\bar{4}2m$	$\bar{4}2'm'$	$4_R m' m'_R$	$2'm_R m'_R$	$m'1'_R$	m'_R	m_R	m'	1
4/mmm (D_{4h})	4/mmm	4mm1 _R	2mm1 _R	2mm1 _R	2 _R mm _R	2 _R mm _R	2 _R mm _R	2 _R
4/mmm	4/mmm1'	4mm1 _R 1'	2mm1 _R 1'	2mm1 _R 1'	2 _R mm _R 1'	2 _R mm _R 1'	2 _R mm _R 1'	2 _R 1'
4/mmm	4'/mmm'	4'mm'1 _R	2mm1 _R	2'mm'1' _R	2 _R mm _R	2 _R mm _R	2 _R m'm'_ _R	2 _R
4/mmm	4/mm'm'	4m'm'1 _R	2'mm'1' _R	2'mm'1' _R	2 _R m'm'_ _R	2 _R mm _R	2 _R m'm'_ _R	2 _R
4/mmm	4/m'm'm'	4m'm'1' _R	2m'm'1' _R	2m'm'1' _R	2'_ _R m'm'_ _R	2'_ _R m'm'_ _R	2'_ _R m'm'_ _R	2'_ _R
4/mmm	4/m'mm	4mm1' _R	2'mm'1 _R	2'mm'1 _R	2'_ _R mm'_ _R	2'_ _R m'm'_ _R	2'_ _R mm'_ _R	2'_ _R
4/mmm	4'/m'm'm	4'mm'1' _R	2m'm'1' _R	2'mm'1 _R	2'_ _R m'm'_ _R	2'_ _R m'm'_ _R	2'_ _R mm'_ _R	2'_ _R

TABLE XII. Assignment of trigonal magnetic point groups to magnetic CBED groups.

PG	mPG	mDG for beam directions	
		[0001]	[<i>uv.w</i>]
3 (C_3)	3	3	1
3	31'	31'	11'
$\bar{3}$ (C_{3i})	$\bar{3}$	6_R	2_R
$\bar{3}$	$\bar{3}1'$	$6_R1'$	$2_R1'$
$\bar{3}$	$\bar{3}'$	$6'_R$	$2'_R$

TABLE XIII. Assignment of trigonal magnetic point groups to magnetic CBED groups (continued).

PG	mPG	mDG for beam directions			
		[0001]	$\langle 11\bar{2}0 \rangle$	[$u\bar{u}.w$]	[<i>uv.w</i>]
32 (D_3)	32	$3m_R$	2	m_R	1
32	321'	$3m_R1'$	21'	m_R1'	11'
32	32'	$3m'_R$	2'	m'_R	1
3m (C_{3v})	3m	3m	1_R	m	1
3m	3m1'	$3m1'$	$1_R1'$	$m1'$	11'
3m	3m'	$3m'$	$1'_R$	m'	1
$\bar{3}m$ (D_{3d})	$\bar{3}m$	6_Rmm_R	21_R	2_Rmm_R	2_R
$\bar{3}m$	$\bar{3}m1'$	$6_Rmm_R1'$	$21_R1'$	$2_Rmm_R1'$	$2_R1'$
$\bar{3}m$	$\bar{3}m'$	$6_Rm'm'_R$	$2'1'_R$	$2_Rm'm'_R$	2_R
$\bar{3}m$	$\bar{3}'m'$	$6'_Rm'm_R$	$2'1'_R$	$2'_Rm'm_R$	$2'_R$
$\bar{3}m$	$\bar{3}'m$	$6'_Rmm'_R$	$2'1_R$	$2'_Rmm'_R$	$2'_R$

TABLE XIV. Assignment of hexagonal magnetic point groups to magnetic CBED groups.

PG	mPG	mDG for beam directions		
		[0001]	[<i>uv.0</i>]	[<i>uv.w</i>]
6 (C_6)	6	6	m_R	1
6	61'	61'	m_R1'	11'
6	6'	6'	m'_R	1
$\bar{6}$ (C_{3h})	$\bar{6}$	31_R	m	1
$\bar{6}$	$\bar{6}1'$	$31_R1'$	$m1'$	11'
$\bar{6}$	$\bar{6}'$	$31'_R$	m'	1
6/m (C_{6h})	6/m	61_R	2_Rmm_R	2_R
6/m	6/m1'	$61_R1'$	$2_Rmm_R1'$	$2_R1'$
6/m	6'/m'	$6'1'_R$	$2_Rm'm'_R$	2_R
6/m	6/m'	$61'_R$	$2'_Rm'm_R$	$2'_R$
6/m	6'/m	$6'1_R$	$2'_Rmm'_R$	$2'_R$

TABLE XV. Assignment of hexagonal magnetic point groups to magnetic CBED groups (continued).

PG	mPG	mDG for beam directions						
		[0001]	$\langle 11\bar{2}0 \rangle$	$\langle 1\bar{1}00 \rangle$	$[uv.0]$	$[uu.w]$	$[u\bar{u}.w]$	$[uv.w]$
622 (D_6)	622	$6m_Rm_R$	$2m_Rm_R$	$2m_Rm_R$	m_R	m_R	m_R	1
622	6221'	$6m_Rm_R1'$	$2m_Rm_R1'$	$2m_Rm_R1'$	m_R1'	m_R1'	m_R1'	11'
622	6'22'	$6'm_Rm'_R$	$2m'_Rm'_R$	$2'm_Rm'_R$	m'_R	m'_R	m_R	1
622	62'2'	$6m'_Rm'_R$	$2'm_Rm'_R$	$2'm_Rm'_R$	m_R	m'_R	m'_R	1
6mm (C_{6v})	6mm	6mm	$m1_R$	$m1_R$	m_R	m	m	1
6mm	6mm1'	6mm1'	$m1_R1'$	$m1_R1'$	m_R1'	$m1'$	$m1'$	11'
6mm	6'mm'	6'mm'	$m'1_R$	$m'1_R$	m'_R	m'	m	1
6mm	6m'm'	6m'm'	$m'1'_R$	$m'1'_R$	m_R	m'	m'	1
$\bar{6}m2$ (D_{3h})	$\bar{6}m2$	$3m1_R$	$m1_R$	$2mm$	m	m_R	m	1
$\bar{6}m2$	$\bar{6}m21'$	$3m1_R1'$	$m1_R1'$	$2mm1'$	$m1'$	m_R1'	$m1'$	11'
$\bar{6}m2$	$\bar{6}'m'2$	$3m'1'_R$	$m'1'_R$	$2m'm'$	m'	m_R	m'	1
$\bar{6}m2$	$\bar{6}'m'2'$	$3m'1'_R$	$m'1_R$	$2'mm'$	m'	m'_R	m	1
$\bar{6}m2$	$\bar{6}m'2'$	$3m'1_R$	$m'1'_R$	$2'mm'$	m	m'_R	m'	1
6/mmm (D_{6h})	6/mmm	$6mm1_R$	$2mm1_R$	$2mm1_R$	2_Rmm_R	2_Rmm_R	2_Rmm_R	2_R
6/mmm	6/mmm1'	$6mm1_R1'$	$2mm1_R1'$	$2mm1_R1'$	$2_Rmm_R1'$	$2_Rmm_R1'$	$2_Rmm_R1'$	$2_R1'$
6/mmm	6'/m'mm'	$6'mm'1'_R$	$2m'm'1_R$	$2'mm'1'_R$	$2_Rm'm'_R$	$2_Rm'm'_R$	2_Rmm_R	2_R
6/mmm	6/mm'm'	$6m'm'1_R$	$2'mm'1'_R$	$2'mm'1'_R$	2_Rmm_R	$2_Rm'm'_R$	$2_Rm'm'_R$	2_R
6/mmm	6/m'm'm'	$6m'm'1'_R$	$2m'm'1'_R$	$2m'm'1'_R$	$2'_Rm'm_R$	$2'_Rm'm_R$	$2'_Rm'm_R$	$2'_R$
6/mmm	6/m'mmm	$6mm1'_R$	$2'mm'1_R$	$2'mm'1_R$	$2'_Rm'm_R$	$2'_Rmm'_R$	$2'_Rmm'_R$	$2'_R$
6/mmm	6'/m'mm'	$6'mm'1_R$	$2'mm'1_R$	$2mm1'_R$	$2'_Rmm'_R$	$2'_Rm'm_R$	$2'_Rmm'_R$	$2'_R$

TABLE XVI. Assignment of cubic magnetic point groups to magnetic CBED groups.

PG	mPG	mDG for beam directions			
		$\langle 100 \rangle$	$\langle 111 \rangle$	$\langle uw0 \rangle$	$[uvw]$
23 (T)	23	$2m_R m_R$	3	m_R	1
23	$231'$	$2m_R m_R 1'$	$31'$	$m_R 1'$	$11'$
$m\bar{3}$ (T_h)	$m\bar{3}$	$2mm1_R$	6_R	$2_R mm_R$	2_R
$m\bar{3}$	$m\bar{3}1'$	$2mm1_R 1'$	$6_R 1'$	$2_R mm_R 1'$	$2_R 1'$
$m\bar{3}$	$m'\bar{3}'$	$2m' m' 1'_R$	$6'_R$	$2'_R m' m'_R$	$2'_R$

TABLE XVII. Assignment of cubic magnetic point groups to magnetic CBED groups (continued).

PG	mPG	mDG for beam directions					
		$\langle 100 \rangle$	$\langle 110 \rangle$	$\langle 111 \rangle$	$\langle uv0 \rangle$	$\langle uuw \rangle$	$[uvw]$
432 (O)	432	$4m_R m_R$	$2m_R m_R$	$3m_R$	m_R	m_R	1
432	$4321'$	$4m_R m_R 1'$	$2m_R m_R 1'$	$3m_R 1'$	$m_R 1'$	$m_R 1'$	$11'$
432	$4'32'$	$4'm_R m'_R$	$2'm_R m'_R$	$3m'_R$	m_R	m'_R	1
$\bar{4}3m$ (T_d)	$\bar{4}3m$	$4_R m m_R$	$m 1_R$	$3m$	m_R	m	1
$\bar{4}3m$	$\bar{4}3m 1'$	$4_R m m_R 1'$	$m 1_R 1'$	$3m 1'$	$m_R 1'$	$m 1'$	$11'$
$\bar{4}3m$	$\bar{4}'3m'$	$4'_R m' m_R$	$m' 1'_R$	$3m'$	m_R	m'	1
$m\bar{3}m$ (O_h)	$m\bar{3}m$	$4mm 1_R$	$2mm 1_R$	$6_R m m_R$	$2_R m m_R$	$2_R m m_R$	2_R
$m\bar{3}m$	$m\bar{3}m 1'$	$4mm 1_R 1'$	$2mm 1_R 1'$	$6_R m m_R 1'$	$2_R m m_R 1'$	$2_R m m_R 1'$	$2_R 1'$
$m\bar{3}m$	$m'\bar{3}'m$	$4'm m' 1'_R$	$2'm m' 1_R$	$6'_R m m'_R$	$2'_R m' m_R$	$2'_R m m'_R$	$2'_R$
$m\bar{3}m$	$m\bar{3}m'$	$4'm m' 1_R$	$2'm m' 1'_R$	$6_R m' m'_R$	$2_R m m_R$	$2_R m' m'_R$	2_R
$m\bar{3}m$	$m'\bar{3}'m'$	$4m' m' 1'_R$	$2m' m' 1'_R$	$6'_R m' m'_R$	$2'_R m' m_R$	$2'_R m' m_R$	$2'_R$

- [1] A. Zamorzaev, Generalization of the Fedorov groups, *Soviet Physics Crystallography* **2**, 10 (1953).
- [2] J. Rodríguez-Carvajal and J. Villain, Magnetic structures, *Comptes Rendus. Physique* **20**, 770 (2019).
- [3] S. Blundell, *Magnetism in Condensed Matter*, Oxford Master Series in Condensed Matter Physics (OUP Oxford, 2001).
- [4] L. Šmejkal, J. Sinova, and T. Jungwirth, Emerging Research Landscape of Altermagnetism, *Phys. Rev. X* **12**, 040501 (2022).
- [5] Y. Tokura, K. Yasuda, and A. Tsukazaki, Magnetic topological insulators, *Nature Reviews Physics* **1**, 126 (2019).
- [6] N. P. Armitage, E. J. Mele, and A. Vishwanath, Weyl and Dirac semimetals in three-dimensional solids, *Rev. Mod. Phys.* **90**, 015001 (2018).
- [7] H. Watanabe, H. C. Po, and A. Vishwanath, Structure and topology of band structures in the 1651 magnetic space groups, *Science advances* **4**, eaat8685 (2018).
- [8] Y. A. Izyumov, V. E. Naish, and R. P. Ozerov, *Neutron Diffraction of Magnetic Materials* (Consultants Bureau, New York, 1991).
- [9] W. Kossel and G. Möllenstedt, Elektroneninterferenzen im konvergenten Bündel, *Ann. Phys. (Leipzig)* **428**, 113 (1939).
- [10] J. Morniroli, G. Ji, and D. Jacob, A systematic method to identify the space group from PED and CBED patterns part I - theory, *Ultramicroscopy* **121**, 42 (2012).
- [11] D. Jacob, G. Ji, and J. Morniroli, A systematic method to identify the space group from PED and CBED patterns part II – practical examples, *Ultramicroscopy* **121**, 61 (2012).
- [12] B. F. Buxton, J. A. Eades, J. W. Steeds, G. M. Rackham, and F. C. Frank, The symmetry of electron diffraction zone axis patterns, *Philos. Trans. R. Soc. London, Ser. A* **281**, 171 (1976).
- [13] M. Tanaka, in *International Tables for Crystallography*, Vol. B (Wiley Online Library, 2010) Chap. 2.5, pp. 307–356.
- [14] P. Goodman and G. Lehmpfuhl, Observation of the breakdown of Friedel’s law in electron diffraction and symmetry determination from zero-layer interactions, *Acta Crystallogr. Sec. A* **24**, 339 (1968).
- [15] M. G. Francesconi, A. L. Kirbyshire, C. Greaves, O. Richard, and G. Van Tendeloo, Synthesis and structure of $\text{Bi}_{14}\text{O}_{20}(\text{SO}_4)$, a new bismuth oxide sulfate, *Chem. Mater.* **10**, 626 (1998).
- [16] K. Tsuda and M. Tanaka, Refinement of crystal structural parameters using two-dimensional energy-filtered CBED patterns, *Acta Crystallogr. Sec. A* **55**, 939 (1999).
- [17] D. Enidjer, A. Venkert, J. Bernstein, and M. Talianker, The structure of a new ternary aluminide $\text{Th}_4\text{Fe}_3\text{Al}_{32}$, *Journal of Alloys and Compounds* **474**, 169 (2009).
- [18] K. Tsuda, A. Yasuhara, and M. Tanaka, Two-dimensional mapping of polarizations of rhombohedral nanostructures in the tetragonal phase of BaTiO_3 by the combined use of the scanning transmission electron microscopy and convergent-beam electron diffraction methods, *Appl. Phys. Lett.* **103**, 082908 (2013).
- [19] Y. Shi, Y. Guo, X. Wang, A. J. Princep, D. Khalyavin, P. Manuel, Y. Michiue, A. Sato, K. Tsuda, S. Yu, M. Arai, Y. Shirako, M. Akaogi, N. Wang, K. Yamaura, and A. T. Boothroyd, A ferroelectric-like structural transition in a metal, *Nat. Mater.* **12**, 1024 (2013).
- [20] T. Hayashida, Y. Uemura, K. Kimura, S. Matsuoka, D. Morikawa, S. Hirose, K. Tsuda, T. Hasegawa, and T. Kimura, Visualization of ferroaxial domains in an order-disorder type ferroaxial crystal, *Nat. Commun.* **11**, 4582 (2020).
- [21] Y. Shen and D. E. Laughlin, Magnetic effects on the symmetry of CBED patterns of ferromagnetic PrCo_5 , *Philos. Mag. Lett.* **62**, 187 (1990).
- [22] J. C. Loudon, Antiferromagnetism in NiO observed by transmission electron diffraction, *Phys. Rev. Lett.* **109**, 267204 (2012).
- [23] Y. Kohno, T. Seki, S. D. Findlay, Y. Ikuhara, and N. Shibata, Real-space visualization of intrinsic magnetic fields of an antiferromagnet, *Nature (London)* **602**, 234 (2022).
- [24] F. Krizek, S. Reimers, Z. Kašpar, A. Marmodoro, J. Michalíčka, O. Man, A. Edström, O. J. Amin, K. W. Edmonds, R. P. Champion, F. Maccherozzi, S. S. Dhesi, J. Zubáč, D. Kriegner, D. Carbone, J. Železný, K. Výborný, K. Olejník, V. Novák, J. Ruzs, J.-C. Idrobo, P. Wadley, and T. Jungwirth, Atomically sharp domain walls in an antiferromagnet, *Sci. Adv.* **8**, eabn3535 (2022).
- [25] K. X. Nguyen, J. Huang, M. H. Karigerasi, K. Kang, D. G. Cahill, J.-M. Zuo, A. Schleife, D. P. Shoemaker, and P. Y. Huang, Angstrom-scale imaging of magnetization in antiferromagnetic Fe_2As via 4D-STEM, *Ultramicroscopy* **247**, 113696 (2023).
- [26] T. Tanigaki, T. Akashi, T. Yoshida, K. Harada, K. Ishizuka, M. Ichimura, K. Mitsuishi, Y. Tomioka, X. Yu, D. Shindo, Y. Tokura, Y. Murakami, and H. Shinada, Electron holography observation of individual ferromagnetic lattice planes, *Nature (London)* **631**, 521 (2024).
- [27] A. Edström, A. Lubk, and J. Ruzs, Magnetic effects in the paraxial regime of elastic electron scattering, *Phys. Rev. B* **94**, 174414 (2016).
- [28] A. Rother and K. Scheerschmidt, Relativistic effects in elastic scattering of electrons in TEM, *Ultramicroscopy* **109**, 154 (2009).
- [29] A. Edström, A. Lubk, and J. Ruzs, Elastic Scattering of Electron Vortex Beams in Magnetic Matter, *Phys. Rev. Lett.* **116**, 127203 (2016).
- [30] D. M. Bird, Theory of zone axis electron diffraction, *Journal of Electron Microscopy Technique* **13**, 77 (1989).
- [31] M. V. Berry, Diffraction in crystals at high energies, *J. Phys. C* **4**, 697 (1971).
- [32] D. Gratias and R. Portier, Time-like perturbation method in high-energy electron diffraction, *Acta Crystallogr. Sec. A* **39**, 576 (1983).
- [33] One can find a purely real representation of all group elements and thereby show that the additional complex conjugation introduced by making z reversal antiunitary does not change the commutation relations.
- [34] E. Wigner, *Gruppentheorie und ihre Anwendung auf die Quantenmechanik der Atomspektren* (Vieweg, Braunschweig, 1931).
- [35] D. B. Litvin, *Magnetic Group Tables* (International Union of Crystallography, 2013).

- [36] C. J. Bradley and B. L. Davies, Magnetic groups and their corepresentations, *Rev. Mod. Phys.* **40**, 359 (1968).
- [37] M. S. S. Dresselhaus, G. Dresselhaus, and A. Jorio, *Group Theory: Application to the Physics of Condensed Matter* (Springer, Berlin, 2008).
- [38] M. De Graef, Visualization of time-reversal symmetry in magnetic point groups, *Metallurgical and Materials Transactions A* **41**, 1321 (2010).
- [39] L.-M. Peng, G. Ren, S. L. Dudarev, and M. J. Whelan, Robust Parameterization of Elastic and Absorptive Electron Atomic Scattering Factors, *Acta Cryst. A* **52**, 257 (1996).
- [40] S. Lee, Y. Ishikawa, P. Miao, S. Torii, T. Ishigaki, and T. Kamiyama, Magnetoelastic coupling forbidden by time-reversal symmetry: Spin-direction-dependent magnetoelastic coupling on MnO, CoO, and NiO, *Phys. Rev. B* **93**, 064429 (2016).
- [41] N. Emery, E. J. Wildman, J. M. S. Skakle, A. C. McLaughlin, R. I. Smith, and A. N. Fitch, Variable temperature study of the crystal and magnetic structures of the giant magnetoresistant materials LMnAsO (L = La, Nd), *Phys. Rev. B* **83**, 144429 (2011).
- [42] J. Á. Castellanos-Reyes, P. Zeiger, A. Bergman, D. Kepaptsoglou, Q. M. Ramasse, J. C. Idrobo, and J. Rusz, Unveiling the impact of temperature on magnon diffuse scattering detection in the transmission electron microscope, *Physical Review B* **108**, 134435 (2023).
- [43] K. Lyon and J. Rusz, Parameterization of magnetic vector potentials and fields for efficient multislice calculations of elastic electron scattering, *Acta Crystallographica Section A: Foundations and Advances* **77**, 509 (2021).
- [44] J. Snarski-Adamski, A. Edström, P. Zeiger, J. Ángel Castellanos-Reyes, K. Lyon, M. Werwiński, and J. Rusz, Simulations of magnetic bragg scattering in transmission electron microscopy, *Ultramicroscopy* **247**, 113698 (2023).
- [45] M. A. McGuire and V. O. Garlea, Short- and long-range magnetic order in lamnaso, *Phys. Rev. B* **93**, 054404 (2016).
- [46] W. L. Roth, Magnetic structures of MnO, FeO, CoO, and NiO, *Phys. Rev.* **110**, 1333 (1958).
- [47] N. Belov, N. Neronova, and T. Smirnova, Shubnikov groups, *Kristallografiya* **2**, 315 (1957).
- [48] R. W. Cairns and E. Ott, X-ray studies of the system nickel–oxygen–water. I. nickelous oxide and hydroxide, *J. Am. Chem. Soc.* **55**, 527 (1933).
- [49] S. Saito, M. Miura, and K. Kurosawa, Optical observations of antiferromagnetic S domains in NiO (111) platelets, *Journal of Physics C: Solid State Physics* **13**, 1513 (1980).
- [50] P. Wadley, B. Howells, J. Železný, C. Andrews, V. Hills, R. P. Campion, V. Novák, K. Olejník, F. Maccheronzi, S. S. Dhesi, S. Y. Martin, T. Wagner, J. Wunderlich, F. Freimuth, Y. Mokrousov, J. Kuneš, J. S. Chauhan, M. J. Grzybowski, A. W. Rushforth, K. W. Edmonds, B. L. Gallagher, and T. Jungwirth, Electrical switching of an antiferromagnet, *Science* **351**, 587 (2016).
- [51] J. Gjønnnes and A. F. Moodie, Extinction conditions in the dynamic theory of electron diffraction, *Acta Crystallographica* **19**, 65 (1965).
- [52] K. Fujiwara, Relativistic theory of electron diffraction, *Journal of the Physical Society of Japan* **16**, 2226 (1961).
- [53] Note that in [12], the point group D_2 is denoted by $mm2$ instead of $2mm$, which we use here. In [35], the point groups C_1 , D_1 , D_2 , and D_3 are denoted by 211 , $1m1$, $2mm$ (like here), and $3m1$, respectively.